

# The effect of near-fault directivity on building seismic collapse risk

Casey Champion<sup>1,\*†</sup> and Abbie Liel<sup>2</sup>

<sup>1</sup>ZFA Structural Engineers, San Francisco, CA, USA

<sup>2</sup>Department of Civil, Environmental and Architectural Engineering Boulder, CO, USA

## SUMMARY

Forward directivity may cause large velocity pulses in ground motion time histories that are damaging to buildings at sites close to faults, potentially increasing seismic collapse risk. This study quantifies the effects of forward directivity on collapse risk through incremental dynamic analysis of building simulation models that are capable of capturing the key aspects of strength and stiffness degradation associated with structural collapse. The paper also describes a method for incorporating the effects of near-fault directivity in probabilistic assessment of seismic collapse risk. The analysis is based on a suite of RC frame models that represent both past and present building code provisions, subjected to a database of near-fault, pulse-like ground motions with varying pulse periods. Results show that the predicted collapse capacity is strongly influenced by variations in pulse period and building ductility; pulse periods that are longer than the first-mode elastic building period tend to be the most damaging. A detailed assessment of seismic collapse risk shows that the predicted probability of collapse in 50 years for modern concrete buildings at a representative near-fault site is approximately 6%, which is significantly higher than the 1% probability in the far-field region targeted by current seismic design maps in the US. Copyright © 2012 John Wiley & Sons, Ltd.

Received 16 March 2011; Revised 13 October 2011; Accepted 24 October 2011

KEY WORDS: near-fault; forward directivity; pulse-like; building collapse

## 1. INTRODUCTION

Although a number of major urban areas worldwide, including San Francisco and Los Angeles, are crisscrossed by large faults, the risk of earthquake-induced collapse for structures located close to faults is poorly understood. In the near-fault region, ground motions sometimes exhibit a large pulse near the beginning of the velocity time history, as illustrated in Figure 1. These pulse-like ground motions may occur at near-fault sites when the fault rupture propagates toward the site and the rupture velocity is similar to the shear wave velocity, leading to constructive interference of the wave front and the arrival of the seismic energy from the rupture in a large amplitude pulse [1]. The occurrence of so-called ‘forward directivity’ effects is more commonly observed in the fault-normal ground motion components than fault-parallel, and the likelihood of pulse occurrence depends on the site-to-source geometry, earthquake magnitude and other characteristics. The effect of forward directivity also decreases with distance from the fault as seismic waves scatter, such that near-fault pulse-like ground motions are unlikely to occur more than 10 to 15 km away from the rupture [2].

Near-fault pulse-like ground motions may induce large displacement and strength demands in structures and increase the risk of earthquake-induced collapse relative to the high seismic, far-field sites that have been the focus of past research on collapse risk (e.g., [3, 4]). Several examples of extensive structural damage from past earthquakes may have been caused by forward directivity. The well-known Olive View Hospital, which sustained significant damage during the San Fernando,

\*Correspondence to: Casey Champion, ZFA Structural Engineers, San Francisco, CA, USA.

†E-mail: caseyc@zfa.com

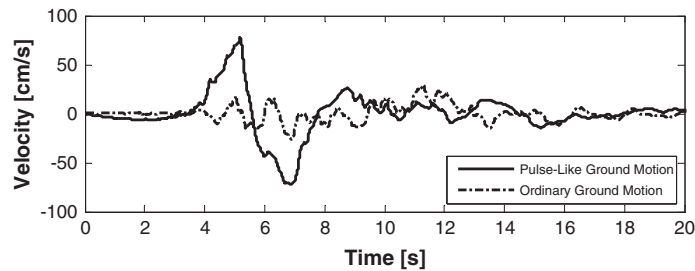


Figure 1. Ground motion record from the 1979 Imperial Valley earthquake (El Centro Array #4), exhibiting a large amplitude pulse early in the velocity time history. For comparison, a nonpulse record from the 1999 Hector Mine earthquake (Hector Station) is also shown.

California (1971) earthquake, is one of the first instances of building collapse that was associated with near-fault directivity [5]. Some structural damage incurred during more recent earthquakes, including Northridge, California (1994), Kobe, Japan (1995), Chi-Chi, Taiwan (1999), and L'Aquila, Italy (2009), was also attributed to the pulse-like ground motions in the near-field.

This study quantifies the impact of near-fault directivity on building seismic collapse risk through dynamic analysis of nonlinear structural simulation models. The suite of building models represent modern and older construction in high seismic regions like California, and include ductile and nonductile RC moment resisting frames. The structures are modeled with material and geometric nonlinear features necessary for simulating the onset of earthquake-induced collapse. The analytical models are subjected to a database of 91 near-fault, pulse-like ground motions with varying pulse periods. Collapse of each structure is predicted from incremental dynamic analysis, in which each ground motion is scaled to increasing intensity until dynamic instability occurs. For each building, this assessment results in a prediction of the probability of collapse as a function of ground motion characteristics, including ground motion intensity (i.e., the spectral acceleration at the first-mode period) and the period of the observed velocity pulse. These fragility functions, which represent structural collapse resistance, are combined with recently developed probabilistic seismic hazard assessments that account for near-fault directivity to quantify the risk of earthquake-induced collapse in the near-field region.

Evaluation of seismic collapse risk in the near-fault region is critical for the continued improvement of building code provisions and seismic hazard maps around the world. In the US, the ASCE 7–10 and the 2012 International Building Code have adopted risk-targeted seismic design maps, which define design spectral acceleration values that are intended to ensure newly designed buildings have a uniform probability of collapse of 1% in 50 years [6]. However, in their current form, these maps do not explicitly account for the higher potential collapse risk in the near-fault region where design ground motion intensities are still based on deterministic values rather than probabilistic seismic hazard analysis. Improved assessment of seismic collapse risk in the near-field is needed to develop the next generation of codes and hazard maps that account more accurately for near-fault directivity effects.

## 2. RESPONSE OF STRUCTURES TO NEAR-FAULT GROUND MOTIONS

The seismic response of structures can be fundamentally different at sites affected by near-fault directivity compared with sites distant from the fault rupture. Past research has examined the dynamic response of both single [5, 7–10] and multiple [11–17] DOF systems in the near-fault region. These studies have predicted elastic and inelastic response of structures subjected to recorded and synthetic pulse-like ground motions. Key conclusions from past research regarding the effect of near-fault ground motions on structural response are summarized as follows:

- (1) Near-fault pulse-like records tend to increase the displacement response in both elastic and inelastic structures relative to nonpulse-like motions [10, 16]. These displacement demands may increase structural and nonstructural damage [12, 15, 17].

- (2) Compared with ordinary far-field records, near-fault pulse-like records tend to cause higher spectral accelerations at longer periods, essentially widening the acceleration-sensitive region of the elastic response spectra [14, 18, 19].
- (3) The ratio of the pulse period in the ground motion velocity time history ( $T_p$ ) to the first-mode period of the building ( $T_1$ ) has a critical effect on structural response [7, 11, 17, 20]. For structures responding in the elastic range, the highest demands will be experienced if  $T_p \approx T_1$  [16]. For ductile structures, the building's effective fundamental period will elongate as damage accumulates. Accordingly, researchers have suggested that ground motion pulses with  $T_p \approx 2 T_1$  may be the most damaging for highly nonlinear systems [8, 12–14, 21, 22]. For taller buildings where  $T_p < T_1$ , the pulse period may coincide with higher modes and cause a traveling wave effect over the height of the building, resulting in large displacement and shear force demands in the upper stories [13, 17, 23].
- (4) As a result of the observations above, the spectral acceleration at the first-mode period, denoted  $S_a(T_1)$ , is an insufficient predictor of structural response at near-fault sites. Researchers have instead proposed the use of ground motion intensity measures such as peak ground velocity, peak ground displacement or inelastic spectral displacement [24, 25]. Vector intensity measures (consisting of spectral acceleration and another parameter) may also be appropriate [11, 12, 17, 20].

### 3. GROUND MOTION DATABASES

This study utilizes a set of 91 pulse-like ground motions from the PEER NGA [26] database compiled by Baker [27]. Baker detects pulses in ground motion records by decomposing the velocity time history into a summation of wavelet basis functions. Ground motions are classified as pulse-like if the amplitude of the extracted wavelet (i.e., the pulse) is large relative to the residual ground motion. In addition, the classification schema verifies that the pulse arrives early in the time history and requires a minimum peak ground velocity of 30 cm/s. The period of the detected velocity pulse is quantified from the dominant frequency of the extracted wavelet. Although other researchers have developed near-fault ground motion databases, this ground motion set is used here because the wavelet analysis methods for pulse identification are quantitative, systematic and, therefore, reproducible.

A complete list of the pulse-like ground motions included in this study can be found in [27]. The records encompass a range of pulse periods from 0.4 to 12.9 s, as shown in Figure 2. The ground motions were recorded from earthquakes with moment magnitudes ranging from 5.0 to 7.6. Although all of the records exhibit velocity pulses, site-to-source distances were not considered in the selection criteria and vary between 0.10 and 102 km. As a result, some of the observed pulses are likely the result of other geological features, such as basins, rather than forward rupture directivity. Nevertheless, all pulse-like records are taken as representative of near-fault ground motions, assuming that large velocity pulses will produce similar structural response regardless of the geologic causal mechanisms. All of the records in the database have been rotated to the fault-normal direction.

An important aspect of this study is the comparison of seismic collapse risk at sites in the near-fault region to sites that are not influenced by forward directivity effects. Therefore, a second set of far-field,

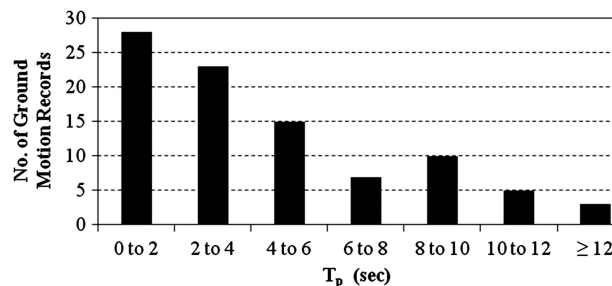


Figure 2. Distribution of pulse periods for ground motion time histories in the near-field database.

nonpulse-like ground motions is also used. The far-field database is based on the FEMA P695 [28] ground motion set, which includes 22 record pairs, each with two horizontal components, for a total of 44 ground motions. However, the wavelet classification algorithm showed that nine of these ground motion records had pulses in the velocity time history. These records were removed from the far-field database and a list of the remaining 35 far-field ground motions used in this study is available in [29]. It should be noted that the far-field records were selected without consideration of spectral shape. Since spectral shape has been shown to have a significant impact on assessed collapse risk [17], results for the far field motions are adjusted to account for the distinct shape of these ground motions, following recommendations in [30].

#### 4. BUILDING DESIGNS AND SIMULATION MODELS

A set of 23 archetypical buildings, designed according to past and present US seismic code provisions, are used to evaluate near-fault seismic collapse risk. The goal of examining a group of structures is to illustrate both the representative effect of near-fault ground motions and the variation in response because of differences in building properties. Although all of the archetype buildings are RC frame structures, they span a range of first mode periods and have varying ductility capacity, such that they represent the building stock more generally in quantifying the relationship between structural properties, pulse period and structural response. Table I(a) lists the design information for each of the building models.

Table I. (a) Design and modeling properties of archetype concrete buildings and (b) collapse capacity results as a function of ground motion pulse period.

| Bldg. ID                                    | (a) Design information |                                       |         | (b) Results: Collapse $S_d(T_1)$ [g] |              |                | All far-field records |
|---|------------------------|---------------------------------------|---------|--------------------------------------|--------------|----------------|-----------------------|
|   | $T_1^a$ (s)            | Design base shear coeff. <sup>b</sup> | $\mu^c$ | At $T_p=0.5 T_1$                     | At $T_p=T_1$ | At $T_p=3 T_1$ |                       |
| <i>Modern (ductile) concrete frames</i>     |                        |                                       |         |                                      |              |                |                       |
| 1P <sup>d</sup>                             | 0.68                   | 0.125                                 | 13.7    | — <sup>e</sup>                       | —            | 1.15           | 2.86                  |
| 1S  | 0.42                   | 0.125                                 | 19.9    | —                                    | —            | 2.87           | 5.46                  |
| 2P  | 0.63                   | 0.125                                 | 19.1    | —                                    | —            | 2.00           | 3.46                  |
| 2S  | 0.60                   | 0.125                                 | 15.0    | —                                    | —            | 2.47           | 4.87                  |
| 4P  | 1.08                   | 0.092                                 | 9.54    | —                                    | 2.70         | 1.13           | 1.75                  |
| 4S  | 0.91                   | 0.092                                 | 10.7    | —                                    | 4.31         | 1.50           | 3.01                  |
| 8P  | 1.69                   | 0.050                                 | 7.86    | 0.68                                 | 1.34         | 0.58           | 1.48                  |
| 8S  | 1.81                   | 0.050                                 | 6.00    | 0.80                                 | 1.55         | 0.37           | 1.59                  |
| 12P   | 1.97                   | 0.044                                 | 9.29    | 0.72                                 | 1.47         | 0.31           | 1.21                  |
| 12S   | 2.15                   | 0.044                                 | 5.42    | 0.62                                 | 1.21         | 0.38           | 1.12                  |
| 20P   | 2.59                   | 0.044                                 | 6.04    | 0.53                                 | 1.19         | 0.35           | 1.01                  |
| 20S   | 2.53                   | 0.044                                 | 6.55    | 0.67                                 | 1.28         | 0.37           | 1.03                  |
| <i>Older (nonductile) concrete frames</i>   |                        |                                       |         |                                      |              |                |                       |
| 2P  | 1.00                   | 0.086                                 | 7.47    | —                                    | 1.16         | 0.51           | 0.83                  |
| 2S  | 1.03                   | 0.086                                 | 3.29    | —                                    | 0.81         | 0.46           | 0.62                  |
| 4P  | 1.89                   | 0.068                                 | 2.47    | 0.37                                 | 0.40         | 0.19           | 0.45                  |
| 4S  | 1.92                   | 0.068                                 | 2.29    | 0.45                                 | 0.47         | 0.22           | 0.43                  |
| 8P  | 2.33                   | 0.054                                 | 1.89    | 0.22                                 | 0.31         | 0.11           | 0.38                  |
| 8S  | 2.23                   | 0.054                                 | 2.25    | 0.36                                 | 0.43         | 0.25           | 0.49                  |
| 12P   | 2.73                   | 0.047                                 | 1.71    | 0.20                                 | 0.25         | 0.17           | 0.30                  |
| 12S   | 2.35                   | 0.047                                 | 2.70    | 0.35                                 | 0.42         | 0.18           | 0.43                  |
| <i>Near-fault (ductile) concrete frames</i> |                        |                                       |         |                                      |              |                |                       |
| 1P  | 0.57                   | 0.150                                 | 17.0    | —                                    | —            | 1.36           | 2.94                  |
| 4P  | 0.81                   | 0.150                                 | 18.3    | —                                    | 6.75         | 2.40           | 3.85                  |
| 20P   | 2.29                   | 0.053                                 | 6.95    | 0.72                                 | 1.33         | 0.40           | 1.57                  |

<sup>a</sup>First-mode period as determined by eigenvalue analysis of the structural model.

<sup>b</sup>Ratio of the design base shear to the effective seismic weight ( $V_{\text{design}}/W_s$ ).

<sup>c</sup>Ductility capacity as determined by nonlinear static pushover analysis. See description below.

<sup>d</sup>Denotes the number of stories in the building with an 'S' or 'P' for space or perimeter frame structures.

<sup>e</sup>Indicates result is not available because of the lack of very short pulse period records in the ground motion set.

Three distinct sets of buildings are considered. The first subset of structures includes 12 modern concrete special moment frames that vary in height from 1 to 20 stories, and include both space and perimeter frame systems. These structures were designed by Haselton *et al.* [3, 31] and satisfy all provisions for special moment frames in modern US building codes [32–34], including strong column–weak beam ratios, shear capacity design requirements, detailing and deflection limits. The structures are designed for a stiff soil site with design spectral accelerations of  $S_{DS} = 1.0 g$  and  $S_{D1} = 0.6 g$ .

The second subset of buildings includes nonductile concrete frames designed by Liel *et al.* [4, 35], ranging in height from 2 to 12 stories. These structures meet the requirements of the 1967 Uniform Building Code, and are therefore representative of older construction in high seismic areas in the US. The design and detailing of these structures is considerably different than that of the modern ductile concrete frames. In particular, the quantity and detailing of transverse reinforcement in beams, columns and joints is insufficient, which reduces ductility capacity and may lead to brittle failure modes. These buildings are of particular interest to the engineering community because of their potential vulnerability to earthquake-induced collapse.

The final set of archetype buildings includes three modern RC special moment frames that are designated as ‘near-fault’ designs. These buildings meet the same design and detailing requirements as the other modern structures, but were designed for 20% to 60% larger seismic forces [28]. These structures provide the opportunity to evaluate the impact of changing the design base shear at near-fault sites.

Probabilistic assessment of seismic collapse risk requires the development of robust analytical models capable of simulating a structure’s principal failure modes. The analyses in this study are conducted using two-dimensional models developed in [3, 4] and implemented in OPENSEES [36]. Each building model consists of a three-bay frame with the appropriate number of stories, as shown in Figure 3. This configuration is taken as a simplified representation of the structural response of a real RC moment frame system, including both interior and exterior columns and joints [31]. P- $\Delta$  effects are incorporated in the model through a leaning column and large deformation geometric transformations.

Beams and columns are modeled using the lumped plasticity (i.e., plastic hinge) approach with the hysteretic model developed by Ibarra *et al.* [37], which was selected for its ability to simulate the strength and stiffness degradation experienced during seismic collapse. The trilinear monotonic backbone curve and corresponding hysteretic behavior of the beam–column element are depicted in Figure 4. An important modeling characteristic is the post-peak response, which captures the strain softening behavior associated with concrete crushing, rebar buckling, and bond failure. This model has been calibrated to experimental tests of more than 250 concrete columns by Haselton *et al.* [38]. Modeling parameters, such as plastic rotation capacity and cyclic deterioration, are obtained from empirical relationships that were developed in the calibration study. The models do not capture the shear-critical response of concrete columns; in the newer structures, shear failure is prevented by capacity design provisions, while in the older buildings, columns are assumed to exhibit combined flexure–shear failure modes that can be captured using the calibrated plastic hinge model. Prediction

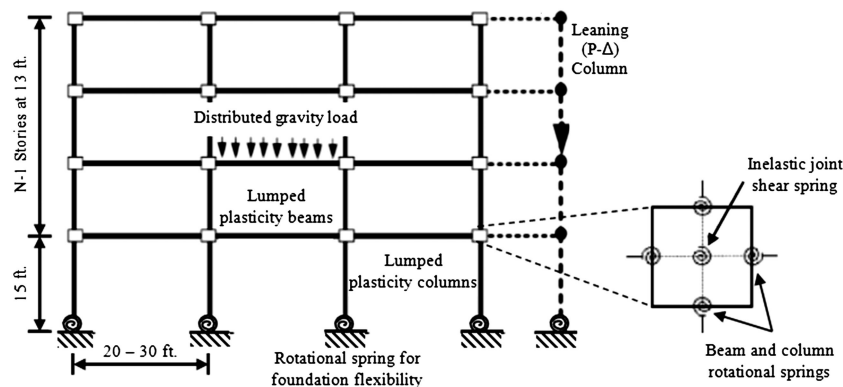


Figure 3. Schematic archetype building model showing key nonlinear elements used for dynamic analysis.

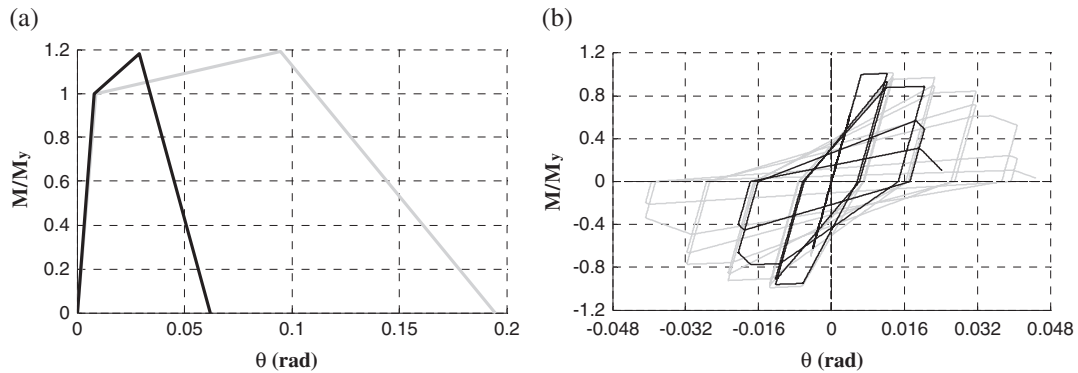


Figure 4. Properties of component model for typical ductile (gray) and nonductile (black) reinforced concrete columns, illustrating differences in (a) monotonic and (b) cyclic behavior [4].

of column shear failure and loss of gravity load bearing capacity in incremental dynamic analysis is progressing with newly developed computational models [39, 40], but is not considered in this study.

A structural system's ability to undergo inelastic deformation before collapse has an important influence on seismic performance. Although there are a number of methods used to quantify ductility or deformation capacity, we follow the procedure outlined in FEMA P695 [28] to calculate a metric of ductility. In this procedure, the results of nonlinear static pushover analysis are used to determine the maximum base shear capacity ( $V_{\max}$ ) and the effective yield displacement ( $\delta_{y,\text{eff}}$ ). The ultimate displacement ( $\delta_u$ ) for the structure is also obtained from pushover analysis and is defined as the displacement on the pushover curve corresponding to 20% strength loss. Ductility ( $\mu$ ) is the ratio of  $\delta_u$  to  $\delta_{y,\text{eff}}$ . The computed ductility capacity for each case study RC frame building is reported in Table I(a), and depends on the detailing of individual components and the structural system configuration. While any measure of deformation capacity is imperfect, the  $\mu$  values reported in Table I(a) provide a metric that can be used to compare differences in near-fault directivity effects for buildings of varying ductility; other measures would show similar trends in the results.

## 5. COLLAPSE ASSESSMENT APPROACH

Seismic collapse risk of each of the archetype buildings is evaluated through incremental dynamic analysis (IDA) [41]. In IDA, the building analytical model is subjected to a selected earthquake time history while tracking the response of the structure (e.g., story displacements, floor accelerations, etc.). The input ground motion is scaled to increasing levels of intensity until collapse occurs, as indicated by runaway interstory drifts. This process is repeated for all earthquake records and for each structure. In this study, the ground motion intensity is scaled by the spectral acceleration at the fundamental period of each building,  $S_a(T_1)$ . Figure 5(a) shows IDA results for a modern 8-story RC building subjected to the suite of far-field ground motions.

Statistics from IDA results are used to derive a fragility curve, illustrated in Figure 5(b), which defines the probability of collapse as a function of the spectral intensity. The collapse fragility function is defined by the median and standard deviation of the ground motion intensities at which collapse occurs in IDA, assuming a lognormal distribution. The lognormal standard deviation ( $\beta$ ) provides a direct measure of the dispersion in the analysis results. Note that the IDA results, as depicted in Figure 5(b), have not yet been adjusted to account for the distinct spectral shape of rare ground motions.

Variability in ground motion characteristics and structural modeling leads to uncertainties in prediction of structural collapse. Record-to-record variability ( $\beta_{\text{RTR}}$ ) is the result of differences in the ground motion frequency content and other geological characteristics, and is quantified by the dispersion computed from the IDA results. Modeling uncertainty reflects the extent to which the simulation model represents the true physical properties and seismic response of a structure, and is

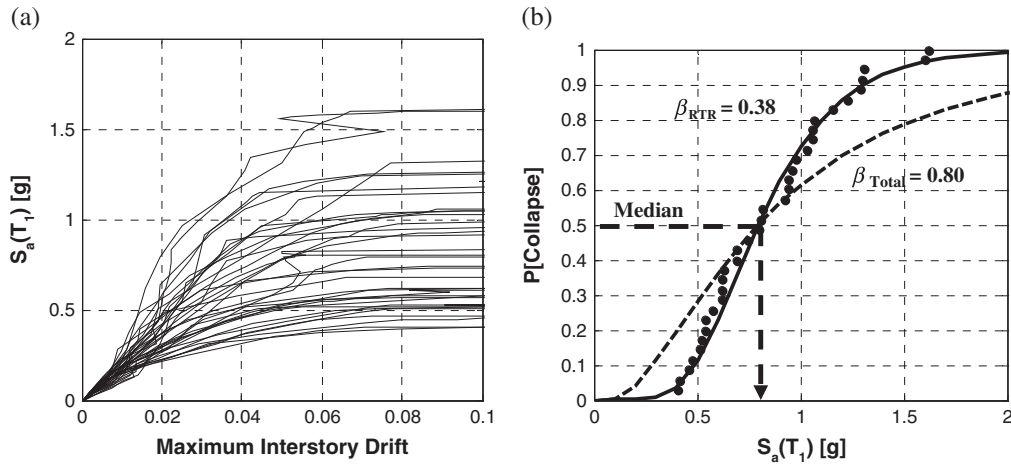


Figure 5. Collapse risk assessment for an 8-story modern concrete frame (Bldg. 8S) subjected to a set of far-field ground motions, showing (a) IDA results and (b) the corresponding collapse fragility function.

especially important for predicting structural collapse. This type of uncertainty stems from nonlinear modeling decisions and the definition of the building model parameters. A variety of methods have been used to account for the effects of modeling uncertainty on seismic fragility curves [42–45]. For the analysis results provided herein, the record-to-record (aleatory) variability and the modeling (epistemic) variability are assumed to be lognormally distributed and independent, such that the total variability is given by the square root of the sum of the squares, or  $\beta_{\text{Total}}^2 = \beta_{\text{RTR}}^2 + \beta_{\text{modeling}}^2$ .  $\beta_{\text{modeling}}$  is taken as approximately 0.65 to generate fragility curves with an assumed lognormal standard deviation of  $\beta_{\text{Total}} = 0.80$ . This value is deemed reasonable for frame systems, and is chosen for ease of comparison with collapse risk assessments used in FEMA P695 [28] and new risk-targeted ground motion maps [6]. This treatment of modeling uncertainties increases the dispersion in the collapse fragility function, as shown in Figure 5(b), but does not change the median. A number of researchers are also working to improve predictions of modeling uncertainties for different types of structures. Other estimates of modeling variability would change the absolute value of collapse risk assessments, but would not significantly affect the relative comparison among different buildings and sites.

For the near-fault ground motions, the collapse risk assessment procedure is modified, as described below, such that the probability of collapse depends both on  $S_a(T_1)$  and the pulse period of the record,  $T_p$ . In doing so, we refine the approach of [12, 17], which considered three distinct ‘bins’ of pulse-like ground motions for records with different pulse periods.

## 6. INFLUENCE OF VELOCITY PULSE ON PREDICTED COLLAPSE CAPACITY

### 6.1. Response of concrete frame buildings

The period of the detected velocity pulse in a near-fault ground motion has a significant impact on building seismic performance. Figure 6(a) illustrates the relationship between pulse period and the collapse capacity for an 8-story modern concrete frame. Each data point represents the collapse capacity for one of the near-fault records obtained from incremental dynamic analysis and is plotted versus the pulse period of that record; larger collapse capacities indicate that the ground motion was scaled to higher intensities before collapse occurred. Figure 6(a) also shows the moving average of the empirical data, computed by averaging the point of interest with the five previous and five subsequent data points. (The number of points used to calculate the moving average does not significantly influence the shape of the computed curve).

The shape of the moving average curve illustrates the impact of different pulses on building collapse capacity. The structure is least susceptible to seismic collapse (i.e., the highest collapse capacities are

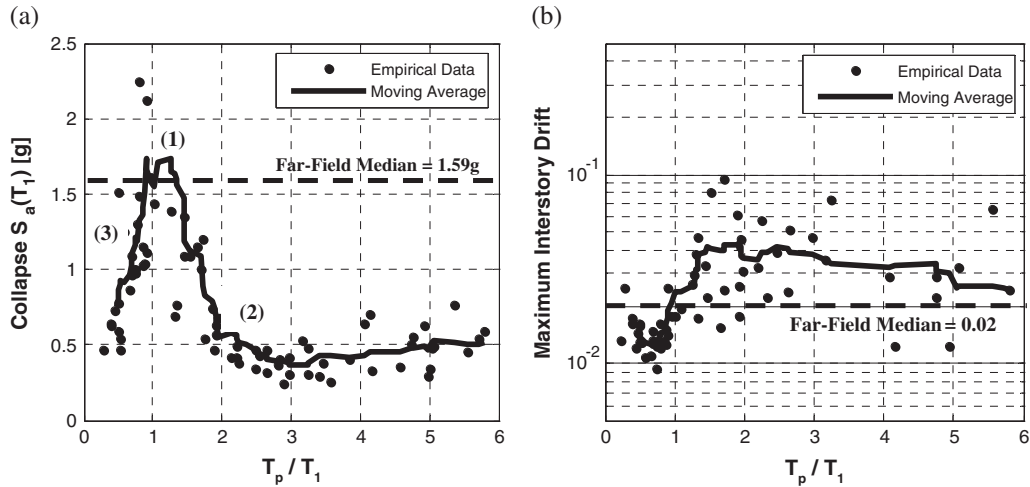


Figure 6. Response of an 8-story modern frame building (Bldg. 8S) subjected to the 91 records in the near-field ground motion database, showing (a) collapse capacity and (b) displacement demand as a function of ground motion pulse period. In (b), all records are scaled to the same intensity,  $S_a(T_1)=0.7g$ .

observed) when the pulse period is approximately equal to the fundamental building period, such that  $T_p/T_1 \approx 1$ . This portion of the curve, labeled (1), may seem counterintuitive because resonance imposes the largest displacement demands in linear-elastic systems. However, structural behavior near collapse is characterized by severely inelastic responses and significant elongation of the effective building period. Accordingly, ground motions with longer pulse periods, or region (2) in Figure 6(a), are the most damaging because they tend to coincide with the effective (lengthened) fundamental period. Region (3) shows decreased collapse resistance when  $T_p < T_1$ , which can be attributed to two factors: shorter pulse periods exciting the structure’s higher modes and high spectral velocities in the shortest pulse period records. The role of higher modes in the response to short-pulse motions is evidenced by more yielding in upper stories than in records with longer period pulses. For comparison, Figure 6(a) also depicts the median collapse capacity for the 8-story building when subjected to the far-field ground motion database (now adjusted for spectral shape).

The relationship between pulse period and displacement demand for the same modern frame building is illustrated in Figure 6(b) for a specified intensity level. The smallest interstory drifts occur in approximately the same pulse period range where the collapse capacity is highest (i.e., where  $T_p \approx T_1$ ).

If we subsequently generate a moving average curve representing the relationship between collapse capacity and ground motion pulse period for each of the archetype buildings, as shown in Figure 7, we see the effect of variations in building deformation capacity. To permit comparison of buildings with

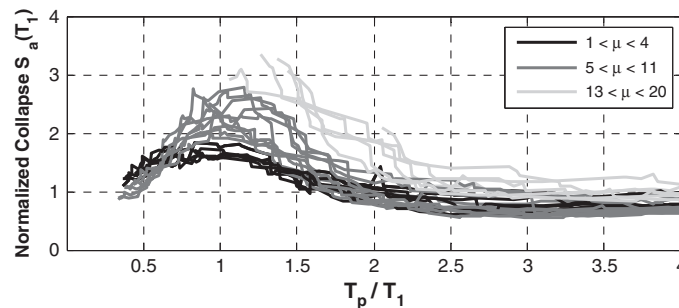


Figure 7. Moving average curves representing collapse capacity as a function of  $T_p / T_1$  for all 23 archetype concrete frame models, illustrating the impact of ground motion pulse period and building deformation capacity on seismic collapse resistance.

different periods, the collapse  $S_a(T_1)$  values forming each moving average curve are normalized by the median collapse  $S_a(T_1)$  for all near-field records of the same curve. When the moving average curves for buildings with different ductility capacities are compared, we observe that all buildings follow the same overall pattern shown in Figure 6(a). However, the least ductile buildings do not exhibit as much variation in collapse resistance with pulse period. The nonductile buildings undergo less substantial period elongation before collapse such that the effective period at collapse is much closer to the elastic first-mode period than for more ductile systems. As a result, the seismic response of these structures is less influenced by regions of the response spectra away from  $T_1$ . There are also many potential failure mechanisms for the nonductile concrete moment frames, such that any pulse period can exploit a weakness in the system. Figure 7 shows that the moving average curves for the most ductile structures, which correspond to the short modern buildings, do not appear to have the same characteristic shape. This difference is due to the short fundamental periods of the buildings ( $0.4 < T_1 < 0.8$  s) and the small number of ground motion records with pulse periods such that  $T_p < T_1$ .

Table I(b) summarizes the collapse results for each of the 23 case study buildings when subjected to the near-field ground motion set. The collapse capacity is reported for multiple pulse periods (expressed as  $T_p = kT_1$ ) to reflect the distinct regions (1), (2) and (3) of response illustrated in Figure 6(a). The median collapse capacity obtained from analysis of the far-field ground motion database is also provided for comparison. The record-to-record variability from the near-fault collapse analysis, computed from residuals between the predicted and observed trends for collapse  $S_a(T_1)$  and  $T_p$ , ranges from 0.24 to 0.41, which is the same order magnitude with those computed in far-field analysis.

### 6.2. Response of single degree-of-freedom systems

To extend the analysis results beyond the suite of building configurations considered, a set of SDOF oscillators was subjected to the same near-field ground motion database and analyzed in OPENSEES using IDA. Each SDOF system is defined by a trilinear backbone curve and associated hysteretic behavior, resulting in oscillators with varying deformation capacities. Each oscillator has a fundamental period of  $T_1 = 1.0$  s, a yield base shear coefficient of 0.075 and a cyclic deterioration level representative of a moderately ductile building. The analysis results, illustrated in Figure 8, confirm the trends described above relating to building deformation capacity, building period, and ground motion pulse period. Not surprisingly, the most ductile SDOF systems have the highest collapse capacity regardless of the pulse period. The more ductile systems also have a larger variation in response as a function of the ground motion pulse period.

### 6.3. Ground motion scaling and spectral shape

By scaling ground motion records to increasing intensity levels, we are able to simulate building response to severe ground motions for which there are a limited number of recordings. However, scaling may introduce a bias in the collapse assessment results because a scaled record may not have the same spectral shape characteristics as a large, rare ground motion [46, 47]. The parameter epsilon ( $\epsilon$ ), which is defined as the number of standard deviations between the observed spectral

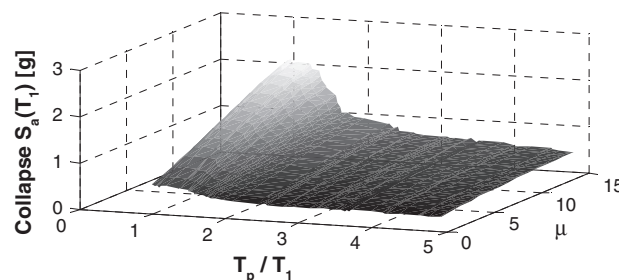


Figure 8. Collapse results for SDOF oscillators as a function of pulse period and deformation capacity ( $\mu$ ).

value and the median value from ground motion prediction equations (for a given building period, earthquake magnitude, and site-to-source distance), can be used as a measure of the ground motion spectral shape. In the far-field region, Baker and Cornell [17] showed that seismic risk assessments that account for both ground motion intensity and epsilon eliminate biases from ground motion scaling.

The ‘residual’ collapse capacity for each of the near-field records is plotted as a function of the ground motion parameter  $\epsilon$  in Figure 9 to investigate the influence of the spectral shape of the pulse-like ground motions on the response of the archetype building models. Since pulse period and spectral shape are related, the difference between the collapse spectral acceleration for a given record and the moving average collapse capacity at that pulse period is calculated for each ground motion to represent the ‘residual’ collapse capacity (i.e., the part that is unexplained by pulse period). Figure 9 does not show a significant trend between  $\epsilon(T_1)$  and the residual collapse capacity, suggesting that a collapse assessment based on both pulse period and spectral acceleration accounts for spectral shape without introducing significant biases due to ground motion scaling. Similar trends were observed for structures with different periods. However, we note there are few records with high  $\epsilon$  values, especially at long periods.

## 7. ASSESSMENT OF SEISMIC COLLAPSE RISK AT NEAR-FIELD SITES

### 7.1. Collapse fragility functions

We now wish to incorporate the effects of near-field directivity in the probabilistic assessment of building seismic collapse risk. As previously shown in Figures 6–8, structural collapse resistance depends not only on ground motion intensity, but also on whether a ground motion time history has a velocity pulse and the corresponding pulse period. Through the theorem of total probability, the probability of collapse for a given spectral acceleration (computed at the first-mode elastic building period),  $P[\text{Coll}|S_a = x]$ , can be written as:

$$P[\text{Col}|S_a = x] = P[\text{Col}|S_a = x, \text{Pulse}] \cdot P[\text{Pulse}|S_a = x] + P[\text{Col}|S_a = x, \text{No Pulse}] \cdot P[\text{No Pulse}|S_a = x] \quad (1)$$

The probability of collapse when no pulse occurs,  $P[\text{Coll}|S_a = x, \text{No Pulse}]$ , is determined from the IDA results for the far-field records. The probability of collapse for pulse-like ground motions,  $P[\text{Coll}|S_a = x, \text{Pulse}]$ , depends on the pulse period and the relative likelihood of different pulse periods occurring:

$$P[\text{Col}|S_a = x, \text{Pulse}] = \sum_{i=1}^{\text{All } T_p} P[\text{Col}|T_p = t_i, S_a = x, \text{Pulse}] \cdot P[T_p = t_i|S_a = x, \text{Pulse}] \quad (2)$$

The probability of collapse associated with each pulse period value,  $P[\text{Coll}|T_p = t_i, S_a = x, \text{Pulse}]$ , is determined from the collapse capacity moving average curve developed for each structure (e.g.,

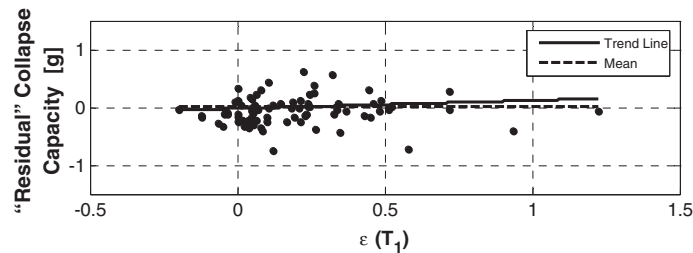


Figure 9. ‘Residual’ collapse capacity as a function of the ground motion parameter  $\epsilon(T_1 = 1.8 \text{ s})$  for an 8-story modern concrete frame (Bldg. 8S) subjected to the near-field ground motions.

Figure 6(a)). If computed in ln-space, the moving average curve represents the median (lognormal mean) of the collapse capacity as a function of  $T_p$ . The probability of collapse is computed for any value of  $T_p$  and  $S_a$  level by assuming a lognormal distribution with the median obtained from the moving average curve at  $T_p$  and the lognormal standard deviation taken as  $\beta_{\text{Total}}=0.80$ . This procedure leads to a collapse fragility curve, represented by Equation (1), which is directly comparable to the far-field fragility curves (Figure 5(b)), but also accounts for the impact of ground motion pulses on collapse behavior.

## 7.2. Probabilistic seismic hazard analysis

In order to assess the risk of earthquake-induced collapse, structural analysis results are combined with probabilistic seismic hazard analysis (PSHA), which can be used to determine the frequency with which a particular ground motion intensity measure (IM) may occur at a site of interest. Equation (3) represents conventional far-field PSHA, showing the calculation of the mean annual frequency ( $\lambda$ ) of exceeding a specific ground motion intensity level ( $x$ ):

$$\lambda_{IM>x} = \sum_{i=1}^N v_i \iint P[IM > x|m, r] f_{M,R}(m, r) dm dr \quad (3)$$

where  $v_i$  is the mean rate of occurrence of earthquakes on a nearby fault  $i$ ,  $N$  is the total number of faults,  $M$  is the moment magnitude,  $R$  is the site-to-source distance and  $f_{M,R}$  is the joint probability density function of  $M$  and  $R$ . The expression  $P[IM > x|m, r]$  is the probability that the ground motion intensity exceeds a particular value,  $x$ , given an earthquake of magnitude  $m$  at distance  $r$ , and can be obtained from ground motion prediction equations. Ground motion intensity is often represented by spectral acceleration at the first-mode period, but other intensity measures can also be used.

Recent research has modified PSHA to incorporate the effects of near-fault, pulse-like ground motions [2, 8, 48]. The near-fault PSHA can be used to compute the mean annual frequency of exceeding a given spectral intensity, accounting for potential near-source directivity through an additional term,  $Z$ , which defines the site-to-source geometry:

$$\lambda_{S_a>x} = \sum_{i=1}^N v_i \iiint P[S_a > x|m, r, z] f_{M,R,Z}(m, r, z) dm dr dz \quad (4)$$

The probability that a particular spectral intensity value is exceeded,  $P[S_a > x|m, r, z]$ , depends on the probability of a pulse occurring, the distribution of possible pulse periods, and the peculiar spectral shape induced by the pulse. The pulse probability is a function of site-to-source geometry, and decreases with distance from the fault and for shorter fault rupture lengths [2, 48]. The pulse period distribution is a function of earthquake magnitude, with larger magnitude events typically causing longer pulse periods [48, 49]. Near-fault PSHA can also be represented as  $\lambda_{S_a=x}$  to allow for combination with the collapse fragility curves. For more details on the equations used to predict pulse probability and the pulse period distribution, the reader is referred to Ref. [48].

Once the probabilistic seismic hazard analysis has been completed for a given spectral intensity level, the hazard can be deaggregated to compute the likelihood that a pulse occurs,  $P[\text{Pulse}|S_a = x]$ , through Equation (5):

$$P[\text{Pulse}|S_a = x] = \lambda_{S_a=x, \text{Pulse}} / \lambda_{S_a=x, \text{Total}} \quad (5)$$

Therefore,  $P[\text{Pulse}|S_a = x]$  represents the ratio of the rate of  $S_a = x$  when only pulse-like ground motions are considered to the total rate of  $S_a = x$ , where both rates are computed from PSHA. This hazard deaggregation is then repeated for each spectral acceleration level of interest. A similar deaggregation process can also be used to identify the pulse periods that most likely produced the spectral value,  $P[T_p = t_i|S_a = x]$ . This hazard information provides the remaining pieces to compute the collapse probability at near-field sites, as defined by Equation (1).

Probabilistic seismic hazard analysis results for a group of case study sites provide the means of examining the impact of variations in site-to-source geometry and building parameters on near-fault collapse risk. In this study, we consider six sites located near the Imperial Valley fault, as shown in Figure 10(a), with site-to-source distances ranging from 5 to 15 km at the end and midpoint of the fault line. These sites are characteristic of high seismic regions where buildings are often located close to a fault rupture. The single fault is 62 km long and is assumed to have a recurrence rate of 0.09 earthquakes per year. The earthquake magnitudes range between 5.0 and 7.0, with the probability distribution of magnitudes modeled using the Youngs and Coppersmith relationship [50]. The location of earthquake epicenters is uniformly distributed along the fault; the rupture direction is random and the rupture extent is proportional to the earthquake magnitude [48]. PSHA results provided by Shahi and Baker [48] are illustrated in Figure 10(b), indicating that larger ground motions are more likely to occur at the sites closest to the fault. Figure 10(c) provides deaggregated hazard results, with the probability of a pulse shown as a function of  $S_a(T_1)$  for each of the midfault sites. A typical distribution of pulse periods is depicted in Figure 10(d).

7.3. Collapse risk assessments including the effects of near-fault directivity

Dynamic analysis results for the suite of RC buildings are used to assess the potential increase in seismic collapse risk due to near-field, pulse-like ground motions. Collapse fragility curves, like those shown

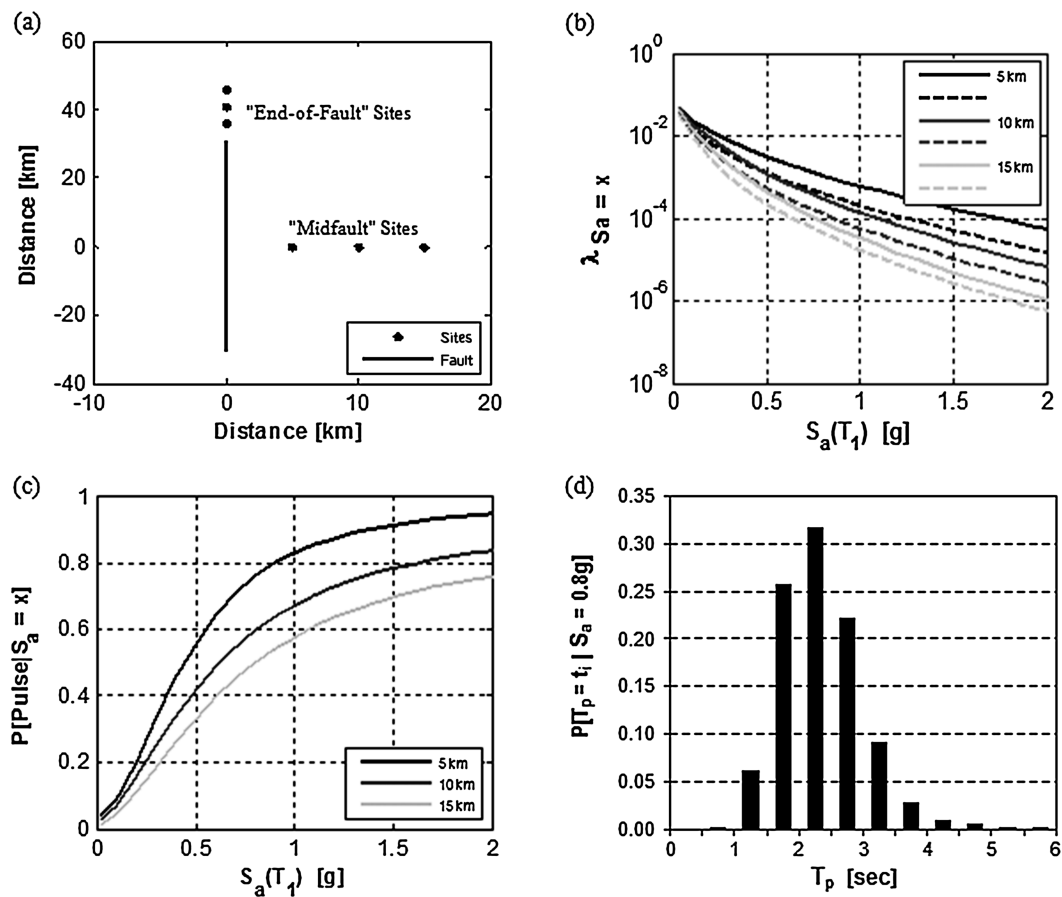


Figure 10. Representative near-field sites considered in Imperial Valley, showing (a) site location and (b) seismic hazard curves for the midfault (solid lines) and end-of-fault (dashed lines) sites with varying site-to-source distances. Hazard deaggregation results show (c) the probability of pulse occurrence for the different midfault sites at  $S_a(T_1) = 1.81$  s and (d) a typical pulse period distribution for one hazard level,  $S_a(T_1) = 0.80$  g, at the 10 km midfault site.

in Figure 11, are developed for all of the archetype buildings at each site, utilizing the probabilistic methods described in Sections 7.1 and 7.2 to incorporate the effects of near-fault directivity. The median collapse capacity results for each of the RC frames are presented in Table II and demonstrate the effect of site-to-source geometry and variations in structural design on the seismic performance of buildings in the near-field region. Note that, for brevity, the analysis results for the case study sites at 10 km are not reported in Table II because they follow the same trends as the 5 and 15 km distant sites.

Table II also includes two additional metrics of seismic risk for the archetype buildings: (1) the probability of collapse in 50 years, and (2) the probability of collapse conditioned on a ground motion intensity that has a 2% probability of being exceeded in 50 years. The probability of collapse in 50 years is computed assuming a Poisson distribution of earthquake occurrences:

$$P[\text{Collapse in 50 years}] = 1 - e^{-\nu t} \tag{6}$$

where  $t$  is the time in years and  $\nu$  is the mean annual frequency of collapse, obtained by integrating the collapse probability distribution with the rate of exceedance for each spectral acceleration and site of interest (i.e., the site-specific seismic hazard curve). The ground motion intensity exceeded with 2% probability in 50 years, denoted  $S_{a,2/50}$ , is obtained from the seismic hazard curve for each site (accounting for pulse-like and nonpulse-like records, and expected values of  $T_p$ ), and is chosen here for comparison of collapse probabilities because it has recently been the basis for design ground motion intensities used in US codes.

As expected, collapse risk tends to decrease with distance from the fault because of the reduction in pulse probability. The contributing pulse period distributions also vary with distance and depend on the earthquake magnitudes that govern the hazard at a particular site. The impact of site-to-source distance is illustrated in the collapse fragility curves in Figure 11 for an 8-story modern, ductile concrete building, which show higher probabilities of collapse for sites closer to the fault. A comparison with the far-field fragility curve (obtained from IDA of the far-field ground motion database) shows that near-fault directivity and pulse effects can reduce the median collapse capacity of this particular concrete frame up to 30%. Figure 11 also demonstrates that the near-field fragility curves approach the far-field curve with increased distance from the fault rupture. The distance at which the near-field curve reaches the far-field curve depends on the first-mode period of the building and nonlinear structural properties. For many of the structures considered, the collapse fragility curve at the 15 km site is very close to the far-field curve; however, in the case of the 8-story ductile building, there is still a relatively high pulse probability at the 15 km site at those spectral accelerations large enough to cause collapse (see Figure 10(c)).

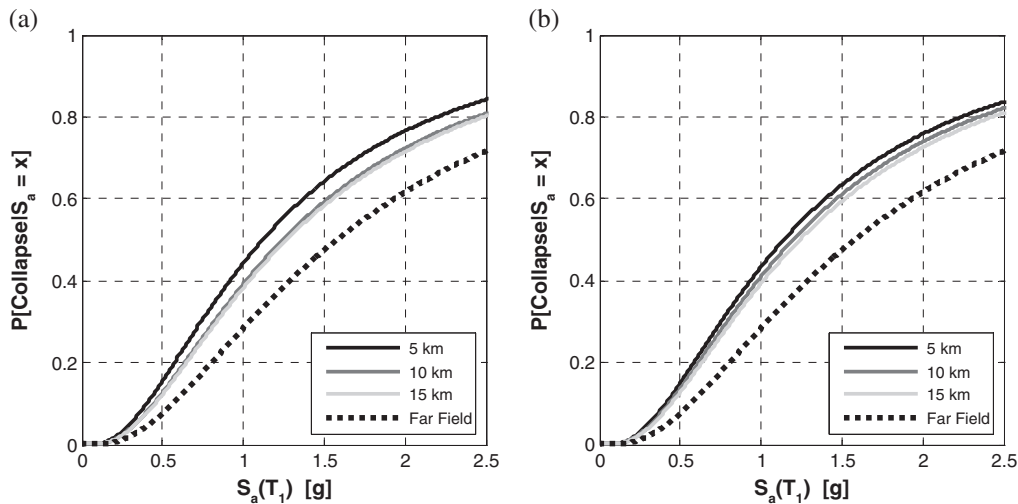


Figure 11. Collapse fragility functions for an 8-story modern ductile building (Bldg. 8S) at three different (a) midfault and (b) end-of-fault sites. The far-field collapse fragility curve is provided for comparison.

Table II. Comparison of metrics of seismic collapse risk for different sites at varying distances from the fault: median collapse capacity, probability of collapse in 50 years, and the probability of collapse conditioned on  $S_{a,2/50}$ .

| Bldg. ID                                    | Median collapse capacity, $S_a(T_1)$ [g] |          |                    |          | $P[\text{Collapse in 50 yrs}]$ |          | $P[\text{Collapse} S_{a,2/50}]$ |          |
|---|--|----------|--------------------|----------|--------------------------------|----------|---------------------------------|----------|
|   | Midfault sites                           |          | End-of-fault sites |          | Midfault sites                 |          | Midfault sites                  |          |
|   | At 5 km                                  | At 15 km | At 5 km            | At 15 km | At 5 km                        | At 15 km | At 5 km                         | At 15 km |
| <i>Modern (ductile) concrete frames</i>     |  |          |                    |          |                                |          |                                 |          |
| 1P  | 2.60                                     | 2.82     | 2.57               | 2.79     | 0.070                          | 0.014    | 0.37                            | 0.11     |
| 1S  | 4.53                                     | 5.36     | 4.34               | 5.18     | 0.034                          | 0.005    | 0.20                            | 0.04     |
| 2P  | 3.38                                     | 3.53     | 3.32               | 3.48     | 0.044                          | 0.009    | 0.26                            | 0.07     |
| 2S  | 4.60                                     | 4.95     | 4.52               | 4.90     | 0.022                          | 0.004    | 0.16                            | 0.03     |
| 4P  | 1.97                                     | 2.01     | 2.01               | 2.06     | 0.061                          | 0.014    | 0.39                            | 0.12     |
| 4S  | 3.24                                     | 3.40     | 3.30               | 3.47     | 0.031                          | 0.005    | 0.22                            | 0.04     |
| 8P  | 0.98                                     | 1.13     | 0.99               | 1.09     | 0.109                          | 0.023    | 0.61                            | 0.19     |
| 8S  | 1.12                                     | 1.27     | 1.14               | 1.24     | 0.077                          | 0.014    | 0.52                            | 0.13     |
| 12P   | 0.93                                     | 1.03     | 0.95               | 1.02     | 0.090                          | 0.019    | 0.57                            | 0.17     |
| 12S   | 0.84                                     | 0.93     | 0.85               | 0.91     | 0.088                          | 0.019    | 0.57                            | 0.17     |
| 20P   | 0.80                                     | 0.87     | 0.81               | 0.85     | 0.061                          | 0.012    | 0.47                            | 0.12     |
| 20S   | 0.91                                     | 0.97     | 0.93               | 0.97     | 0.052                          | 0.010    | 0.42                            | 0.10     |
| <i>Older (nonductile) concrete frames</i>   |  |          |                    |          |                                |          |                                 |          |
| 2P  | 0.81                                     | 0.83     | 0.81               | 0.84     | 0.26                           | 0.10     | 0.81                            | 0.49     |
| 2S  | 0.61                                     | 0.62     | 0.61               | 0.62     | 0.35                           | 0.16     | 0.88                            | 0.62     |
| 4P  | 0.37                                     | 0.40     | 0.37               | 0.39     | 0.31                           | 0.13     | 0.92                            | 0.61     |
| 4S  | 0.38                                     | 0.40     | 0.38               | 0.40     | 0.29                           | 0.13     | 0.91                            | 0.60     |
| 8P  | 0.29                                     | 0.32     | 0.29               | 0.31     | 0.29                           | 0.12     | 0.92                            | 0.59     |
| 8S  | 0.38                                     | 0.41     | 0.38               | 0.40     | 0.24                           | 0.09     | 0.87                            | 0.49     |
| 12P   | 0.24                                     | 0.27     | 0.25               | 0.26     | 0.27                           | 0.12     | 0.91                            | 0.57     |
| 12S   | 0.35                                     | 0.38     | 0.35               | 0.37     | 0.24                           | 0.09     | 0.87                            | 0.50     |
| <i>Near-fault (ductile) concrete frames</i> |  |          |                    |          |                                |          |                                 |          |
| 1P  | 2.74                                     | 2.91     | 2.70               | 2.87     | 0.075                          | 0.017    | 0.12                            | 0.02     |
| 4P  | 4.71                                     | 4.92     | 4.77               | 4.96     | 0.015                          | 0.002    | 0.37                            | 0.13     |
| 20P   | 1.00                                     | 1.17     | 1.02               | 1.12     | 0.056                          | 0.009    | 0.44                            | 0.09     |

A trend indicating decreased seismic risk with distance from the fault is also apparent in the results for both the probability of collapse in 50 years and the collapse probability conditioned on  $S_{a,2/50}$ . For the modern buildings, the computed probability of the structure collapsing in 50 years ranges between 2% and 11% at the closest midfault site, which is a factor of five to eight times higher than that at the most distant site. Similarly, the collapse probabilities conditioned on  $S_{a,2/50}$  vary by a factor of three to five over the 15 km distances considered.

If we compare the collapse risk at each of the midfault and end-of-fault sites for a particular building, we observe that the seismic response is not as largely influenced by the position of the site relative to the fault axis as it is by the distance to the fault rupture. The median collapse capacity results shown in Table II vary less than 5% for equidistant end-of-fault and midfault sites (and in many nonductile structures the difference is much less). The likelihood of pulse-like ground motions occurring at a particular location depends not only on site-to-source geometry, but also on the specific characteristics of the fault rupture mechanism, such as the rupture length and direction. For this geometry, the end-of-fault sites have slightly larger pulse probabilities because of the rupture directivity toward these sites [48]. In addition, the effect of the two-dimensional frames' orientation with respect to the fault rupture was considered, including building (weak-axis) orientations rotated 0°, 45°, and 90° from the fault axis. Although the pulse probability can vary depending on orientation relative to the fault [48], the sensitivity analyses we conducted showed a minor difference in the computed collapse fragility functions when the orientation of the building was altered. As a result, all of the following analysis results presented herein are for the building weak-axis oriented orthogonally to the fault.

A direct comparison of the modern and older RC frames (for buildings of the same height) shows a substantial difference in the predicted collapse capacity results, indicating the higher collapse risk of the older, nonductile concrete structures. The probability of the building collapsing in 50 years is

approximately five times higher for the older RC frames when compared with the modern frames at the site 5 km from the fault, and eight times higher at the 15 km distant site. However, the variations in collapse risk with distance from the fault are less significant for the older, nonductile buildings. Whereas the modern ductile buildings exhibit a 10 to 15% increase in median collapse resistance between the closest and farthest near-field site, the increase is less than 5% for nearly all of the nonductile structures because of the lesser sensitivity of these buildings to ground motion pulse period. Given the many sources of uncertainty in prediction of collapse risk, a 5% difference in collapse capacity for the nonductile buildings is probably not critical. These results also suggest that the collapse risk of even more brittle buildings than those considered here (e.g., nonductile concrete frames with shear-critical columns) would be relatively unaffected by the differences between pulse and nonpulse motions in the near-field, though the overall (absolute) collapse risk is likely higher.

The computed collapse capacity values shown in Table II for the ‘near-fault’ buildings (i.e., the modern buildings designed for larger base shear forces) are 5% to 140% higher than the structures designed for current code levels. The most significant improvement is apparent in the 4-story building, which was also designed for the largest increase in base shear (60% larger than current code requirements). Given the limited number of ‘near-fault’ designs, additional analysis with a larger suite of buildings is needed to better determine how increased seismic design forces could be appropriately used to reduce collapse risk in the near-fault region.

In addition to the structure’s deformation capacity and seismic design forces, the number of stories in a building can significantly influence the prediction of structural collapse. Figure 12 shows the average probability of collapse in 50 years as a function of building height for the ductile and nonductile concrete frames. The magnitude of near-fault directivity effects on structural collapse risk varies with building height, in part because the seismic hazard at different building periods depends on distinct pulse period distributions. Since ground motions with small pulse periods are typically caused by lower magnitude earthquakes, shorter pulse periods (e.g.,  $T_p < 0.5$  s) do not contribute significantly to the collapse risk. As a result, the response of the short-period buildings is largely dominated by pulses with  $T_p > T_1$  since all other pulse periods are unlikely to occur at large  $S_a$  levels. For the midperiod (i.e., 4-story) structures, the response is dominated by pulses with  $T_p \approx T_1$  and  $T_p > T_1$ , with little influence from the higher mode region of response. Incidentally, short pulse periods ( $T_p < 0.6$  s) were excluded from both the hazard and structural analyses, but this exclusion is not expected to affect the results.

#### 7.4. Significance of near-fault directivity in structural and seismic hazard analysis

The calculated metrics of near-fault collapse risk for each building require both site-specific hazard curves and site-specific collapse fragility functions, reflecting modifications in both the structural and seismic hazard analysis to account for pulse-like ground motions. To investigate the importance of these changes, the probability of collapse in 50 years is first recalculated using conventional (nonpulse) hazard curves and the near-field collapse fragility functions. As shown by the dashed lines in Figure 13, the predicted collapse rate decreases when pulse-like ground motions are not

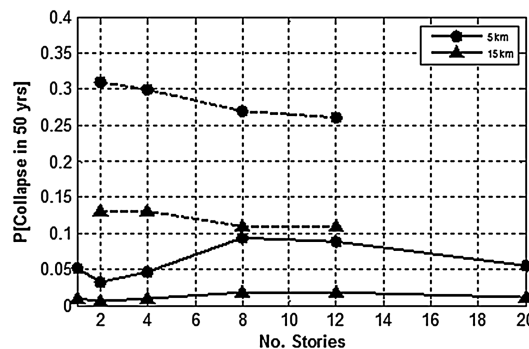


Figure 12. Average probability of collapse as a function of building height for modern ductile (solid lines) and older nonductile (dashed lines) concrete frames at the representative midfault sites.

considered in the development of site-specific hazard curves. The taller buildings show approximately a 10 to 35% underestimation of the collapse probability, while the 1 and 2-story structures exhibit a smaller (less than 5%) variation.

In Figure 13, we also consider the effect of including near-fault directivity in the hazard analysis, but not in the collapse fragility function (i.e., using the far-field fragility functions instead). The most significant differences are observed in the midheight and taller structures. In general, neglecting near-fault directivity in either the structural or seismic hazard analysis leads to an underestimation of collapse risk. A notable exception is the 4-story buildings in Figure 13, for which the near-field fragility function actually has a higher median collapse capacity because of the relatively large contribution from pulse periods with  $T_p \approx T_1$  for buildings with first-mode periods of about 1.0 s.

The collapse risk assessments included in this study clearly depend on the computation of the ground motion hazard. The probabilistic seismic hazard analysis that provides the basis for the risk assessment is different from conventional hazard analysis in that it explicitly accounts for the occurrence of velocity pulses. Other differences include the consideration of a single dominant fault and the use of one ground motion prediction equation, as opposed to a logic-tree combination of different equations. Therefore, although the metrics of collapse risk presented herein are reasonable and the relative trends observed in the collapse metrics (including those showing the effect of site-to-source distance, building height, deformation capacity, etc.) are not expected to change significantly with computational differences, there may be some variation in the absolute value of results if other hazard calculations were used.

## 8. CONCLUSIONS AND IMPLICATIONS

This study examines the impact of near-fault directivity on building seismic collapse risk through dynamic analysis of nonlinear structural simulation models. The analysis is based on a suite of 23 RC buildings that represent modern and older construction in high seismic regions like California. Although all the structures are concrete frames, they encompass a range of building periods and deformation capacities, and more generally represent the effect of pulse-like ground motions on seismic collapse risk. This effort builds on past research on structural response to pulse-like ground motions, and for the first time quantifies collapse risk in the near-field region by combining nonlinear simulation models with new probabilistic seismic hazard analysis results that include forward directivity.

The analysis results show that the seismic collapse behavior of buildings in the near-fault region is governed by the ratio of the ground motion pulse period to the first-mode period of the building,  $T_p/T_1$ . Certain pulse-like records, specifically those with  $T_p/T_1 \geq 2$ , can be shown to cause a substantial decrease in the collapse capacity relative to a suite of far-field ground motions. These long-period pulses tend to coincide with the effective (lengthened) building period and correspond to an average

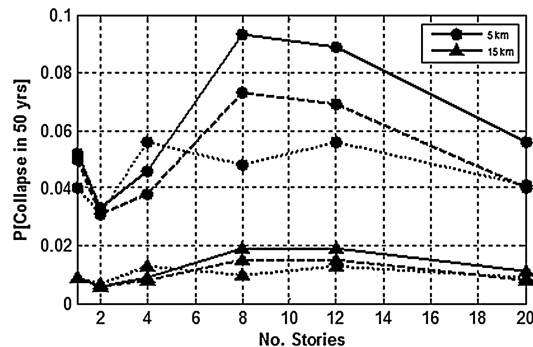


Figure 13. Average probability of collapse as a function of building height showing the impact of not considering near-fault directivity in the hazard analysis (dashed lines) and the impact of not considering near-fault directivity in the structural analysis (dotted lines). The solid lines shown include near-fault directivity in both hazard and structural analyses.

reduction of 55% in collapse capacity when compared with the far-field median. However, for pulse-like records with  $T_p/T_1 \approx 1$ , the building's collapse capacity tends to be on average 13% larger than the far-field results. The analysis also showed variation in these patterns with buildings of different periods or ductility capacities. The effect of  $T_p/T_1$  on collapse capacity is largest for the most ductile buildings, while the older, nonductile structures are less sensitive to variations in pulse period because they experience substantially less period elongation before collapse.

Probabilistic assessments of structural collapse show that accounting for near-fault directivity increases the metrics of seismic risk. At the case study site closest to the fault rupture, collapse probabilities conditioned on the 2% in 50-year ground motion intensity range from 16% to 61% for the modern buildings and 81% to 92% for the older buildings. These values correspond to an average probability of collapse in 50 years of 6% for modern concrete buildings at the closest site to the fault rupture, compared with an average 0.7% probability of collapse in 50 years at the site 15 km from the fault. Conversely, the older buildings have an average probability of collapse in 50 years of 24% at the 5 km distant site and 7% at the farthest site. When the design base shear of the modern buildings is increased, as with the so-called 'near-fault' frames, a significant decrease is observed in collapse probabilities for the 4-story buildings; however, the impact is less significant for the 20-story buildings. Additional analysis is required to determine how increased seismic design forces could be employed to reduce seismic collapse risk in the near-fault region.

The study also shows the importance of considering near-fault directivity in both the probabilistic seismic hazard analysis and the building response simulation. When the effects of forward directivity and pulse-like ground motions are not included in the building fragility curve, the probability of collapse in 50 years can be underestimated by as much as 50% for modern, ductile frames and up to 30% for the older buildings. The magnitude of the relative difference depends on the building period, deformation capacity, and site-to-source geometry.

Detailed assessments of seismic collapse risk in the near-fault region contribute to the continued improvement of seismic hazard maps and building code provisions. Current US seismic codes determine the design base shear from the code-defined MCE (maximum considered earthquake) intensity. Until recently, the MCE was defined at most sites by the ground motion intensity that has a 2% probability of exceedance in 50 years (or a 2475-year mean return period). For sites near known active faults, such as those in coastal California, deterministic MCE values are calculated using ground motion prediction models from characteristic magnitude earthquakes [51]. The 2010 version of ASCE 7 and the 2012 International Building Code have adopted new risk-targeted design maps, which introduce design values, denoted  $MCE_R$ , that are based on a uniform target probability of collapse of 1% in 50 years at sites across the US [6]. Despite the shift to a risk-targeted approach, the new seismic hazard maps do not explicitly consider the collapse risk in the near-fault region, where the MCE intensity is still based on deterministic values. Results herein suggest that the collapse risk of modern, code-compliant buildings in these regions may be significantly higher than the 1% probability of collapse in the 50-year target designated for typical far-field sites. Additional research could be used to confirm these findings more generally, for example, at sites where the seismic hazard is affected by multiple faults.

#### ACKNOWLEDGEMENTS

This research was supported by the US Geological Survey (USGS), Department of the Interior, under USGS award number *G10AP00041*. The views and conclusions contained in this document are those of the authors and should not be interpreted as necessarily representing the official policies, either expressed or implied, of the US Government. The authors would also like to thank Jack Baker and Shrey Shahi, for providing probabilistic seismic hazard data at the near-field sites, Curt Haselton, for providing models of modern concrete buildings, Joseph Ambrosich, for analyzing the single-degree-of-freedom systems, and the two anonymous reviewers for their thoughtful suggestions that improved the quality of the manuscript.

#### REFERENCES

1. Somerville PG, Smith NF, Graves RW, Abrahamson NA. Modification of Empirical Strong Ground Motion Attenuation Relations to Include the Amplitude and Duration Effects of Rupture Directivity. *Seismological Research Letters* 1997; **68**(1):199–222.

2. Iervolino I, Cornell CA. Probability of Occurrence of Velocity Pulses in Near-Source Ground Motions. *Bulletin of the Seismological Society of America* 2008; **98**(5):2262–2277.
3. Haselton CB, Liel AB, Deierlein GG, Dean BS, Chou JH. Seismic Collapse Safety of Reinforced Concrete Buildings: I. Assessment of Ductile Moment Frames. *Journal of Structural Engineering* 2011; **137**(4):481–491.
4. Liel AB, Haselton CB, Deierlein GG. Seismic Collapse Safety of Reinforced Concrete Buildings: II. Comparative Assessment of Non-Ductile and Ductile Moment Frames. *Journal of Structural Engineering* 2011; **137**(4):492–502.
5. Chopra AK, Chintanapakdee C. Comparing response of SDF systems to near-fault and far-fault earthquake motions in the context of spectral regions. *Earthquake Engineering and Structural Dynamics* 2001; **30**:1769–1789.
6. Luco N, Ellingwood BR, Hamburger RO et al. Risk-Targeted versus Current Seismic Design Maps for the Conterminous United States. SEAOC 2007 Convention Proceedings, 2007.
7. Mavroeidis GP, Dong G, Papageorgiou AS. Near-fault ground motions and the response of elastic and inelastic single-degree-of-freedom (SDOF) systems. *Earthquake Engineering and Structural Dynamics* 2004; **33**:1023–1049.
8. Tothong P, Cornell CA, Baker JW. Explicit Directivity-Pulse Inclusion in Probabilistic Seismic Hazard Analysis. *Earthquake Spectra* 2007; **23**(4):867–891.
9. Malhotra P. Response of Buildings to Near-Field Pulse-Like Ground Motions. *Earthquake Engineering and Structural Dynamics* 1999; **28**:1309–1326.
10. MacRae GA, Morrow DV, Roeder CW. Near-Fault Ground Motion Effects on Simple Structures. *Journal of Structural Engineering* 2001; **127**(9):996–1004.
11. Luco N, Cornell CA. Structure-Specific Scalar Intensity Measures for Near-Source and Ordinary Earthquake Ground Motions. *Earthquake Spectra* 2007; **23**(2):357–392.
12. Tothong P, Cornell CA. Structural performance assessment under near-source pulse-like ground motions using advanced ground motion intensity measures. *Earthquake Engineering and Structural Dynamics* 2008; **37**:1013–1037.
13. Krawinkler H, Medina R, Alavi B. Seismic drift and ductility demands and their dependence on ground motions. *Engineering Structures* 2003; **25**:637–653.
14. Alavi B, Krawinkler H. Behavior of moment-resisting frame structures subjected to near-fault ground motions. *Earthquake Engineering and Structural Dynamics* 2004; **33**:687–706.
15. Hall JF, Heaton TH, Halling MW, Wald DJ. Near-Source Ground Motion and its Effects on Flexible Buildings. *Earthquake Spectra* 1995; **11**(4):569–605.
16. Akkar S, Yazgan U, Gulkan P. Drift Estimates in Frame Buildings Subjected to Near-Fault Ground Motions. *Journal of Structural Engineering* 2005; **131**(7):1014–1024.
17. Baker JW, Cornell CA. Vector-valued intensity measures for pulse-like near-fault ground motions. *Engineering Structures* 2008; **30**:1048–1057.
18. Longjun X, Rodriguez-Marek A, Lili X. Design spectra including the effect of rupture directivity in the near-fault region. *Earthquake Engineering and Engineering Vibration* 2006; **5**(2):159–170.
19. Huang YN, Whittaker AS, Luco N. Maximum Spectral Demands in the Near-Fault Region. *Earthquake Spectra* 2008; **24**(1):319–341.
20. Tothong P, Luco N. Probabilistic seismic demand analysis using advanced ground motion intensity measures. *Earthquake Engineering and Structural Dynamics* 2007; **36**:1837–1860.
21. Chioccarelli E, Iervolino I. Near-source seismic demand and pulse-like records: A discussion for L'Aquila earthquake. *Earthquake Engineering and Structural Dynamics* 2010; **39**:1039–1062.
22. Ruiz-Garcia J. Inelastic Displacement Ratios for Seismic Assessment of Structures Subjected to Forward-Directivity Near-Fault Ground Motions. *Journal of Earthquake Engineering* 2011; **15**:449–468.
23. Iwan WD. Drift Spectrum: Measure of Demand for Earthquake Ground Motions. *Journal of Structural Engineering* 1997; **123**(4):397–404.
24. Yamada M, Olsen AH, Heaton TH. Statistical Features of Short-Period and Log-Period Near-Source Ground Motions. *Bulletin of the Seismological Society of America* 2009; **99**(6):3264–3274.
25. Sehatti R, Rodriguez-Marek A, Elgawady M, Cofer WF. Effects of near-fault ground motions and equivalent pulses on multi-story structures. *Engineering Structures* 2011; **33**(3):767–779.
26. Pacific Earthquake Engineering Research Center. NGA Database. <http://peer.berkeley.edu/nga/> [Accessed on June 26, 2009].
27. Baker JW. Quantitative Classification of Near-Fault Ground Motions Using Wavelet Analysis. *Bulletin of the Seismological Society of America* 2007; **97**(5):1486–1501.
28. Applied Technology Council. *Quantification of Building Seismic Performance Factors (FEMA P695)*. FEMA: Redwood City, CA, 2009.
29. Champion C. The Effect of Near-Fault Directivity on Building Seismic Collapse Risk. MS Thesis, University of Colorado at Boulder, 2010.
30. Haselton CB, Baker JW, Liel AB, Deierlein GG. Accounting for Ground Motion Spectral Shape Characteristics in Structural Collapse Assessment Through an Adjustment for Epsilon. *Journal of Structural Engineering* 2011; **137**(3):332–344.
31. Haselton CB, Deierlein GG. Assessing Seismic Collapse Safety of Modern Reinforced Concrete Frame Buildings. Blume Center Technical Report No. 156, 2007.
32. International Code Council. *International Building Code*. Washington, DC, 2003.
33. American Society of Civil Engineers. Minimum Design Loads for Buildings and Other Structures (ASCE 7–05); 2005.

34. American Concrete Institute. Building Code Requirements for Structural Concrete (ACI 318-02); 2002.
35. Liel AB, Deierlein GG. Assessing the Collapse Risk of California's Existing Reinforced Concrete Frame Structures: Metrics for Seismic Safety Decisions. Blume Center Technical Report No. 166, 2008.
36. Pacific Earthquake Engineering Research Center. OpenSees (Open System for Earthquake Engineering Simulation). Berkeley, CA; 2006. <http://opensees.berkeley.edu/index.php> [Accessed on June 26, 2009].
37. Ibarra LF, Medina RA, Krawinkler H. Hysteretic models that incorporate strength and stiffness deterioration. *Earthquake Engineering and Structural Dynamics* 2005; **34**:1489–1511.
38. Haselton CB, Liel AB, Lange ST, Deierlein GG. Beam-Column Element Model Calibrated for Predicting Flexural Response Leading to Global Collapse of RC Frame Buildings. Pacific Earthquake Engineering Center 2007/03, University of California at Berkeley; 2008.
39. Ghannoum WM, Moehle JP, Bozorgnia Y. Analytical Collapse Study of Lightly Confined Reinforced Concrete Frames Subjected to Northridge Earthquake Ground Motions. *Journal of Earthquake Engineering* 2008; **12**(7):1105–1119.
40. Elwood K. Modeling failures in existing reinforced concrete columns. *Canadian Journal of Civil Engineering* 2004; **31**(5):846–859.
41. Vamvatsikos D, Cornell CA. Incremental Dynamic Analysis. *Earthquake Engineering and Structural Dynamics* 2002; **31**:491–514.
42. Liel AB, Haselton CB, Deierlein GG, Baker JW. Incorporating Modeling Uncertainties in the Assessment of Seismic Collapse Risk of Buildings. *Structural Safety* 2009; **31**(2):197–211.
43. Dolsek M. Incremental dynamic analysis with consideration of modeling uncertainties. *Earthquake Engineering and Structural Dynamics* 2009; **38**:805–825.
44. Igusa T, Buonopane SG, Ellingwood BR. Bayesian analysis of uncertainty for structural engineering applications. *Structural Safety* 2002; **24**:165–186.
45. Fragiadakis M, Vamvatsikos D. Performance Uncertainty Estimation using Static Pushover Methods. *Earthquake Engineering and Structural Dynamics* 2009; **00**:1–6.
46. Baker JW. Measuring Bias in Structural Response Caused by Ground Motion Scaling. 8<sup>th</sup> Pacific Conference on Earthquake Engineering, Singapore, 2007; Paper No. 56.
47. Luco N, Bazzurro P. Does amplitude scaling of ground motion records result in biased nonlinear structural drift responses? *Earthquake Engineering and Structural Dynamics* 2007; **36**:1813–1835.
48. Shahi SK, Baker JW. An Empirically Calibrated Framework for Including the Effects of Near Fault Directivity in Probabilistic Seismic Hazard Analysis. *Bulletin of the Seismological Society of America* 2011; **101**(2):742–755.
49. Somerville PG. Magnitude Scaling of the Near Fault Rupture Directivity Pulse. *Physics of the Earth and Planetary Interiors* 2003; **137**(1):201–212.
50. Youngs RR, Coppersmith K. Implications of fault slip rates and earthquake recurrence models to probabilistic seismic hazard analysis. *Bulletin of the Seismological Society of America* 1985; **75**(4):939–964.
51. Building Seismic Safety Council. *NEHRP Recommended Provisions for Seismic Regulations for New Buildings and Other Structures (FEMA 450, 2003 Edition)*. FEMA: Washington, DC, 2004.